Synthesis of ZnO Nanoparticles Assisted by N Sources and their Application in the Photodegradation of Organic Contaminants

Gelson T. S. T. da Silva[+],[a, b] Kele T. G. Carvalho[+],[b] Osmando F. Lopes[+],[a, b] Eliziana S. Gomes,[c] Andréa R. Malagutti,[c] Valmor R. Mastelaro,[d] Caue Ribeiro,*[b] and Henrique A. J. L. Mourão[e]

A modified polymeric precursor method assisted by N sources (urea or melamine) was used to obtain anion-doped ZnO nanoparticles. The influence of these molecules on the physical-chemical and photocatalytic properties of the as-synthesized samples was investigated. The ZnO nanoparticles exhibited a hexagonal wurtzite phase and crystallite sizes of approximately 20 nm. The addition of urea or melamine to the Zn^{2+} precursor solution improved the surface properties of the materials and resulted in controlled growth of the N-doped ZnO nanoparticles, with urea showing superior performance for this purpose. These changes led to improved photocatalytic performance in the degradation of methylene blue (MB) dye and ethionamide antibiotic under UVC irradiation. It was observed that the indirect mechanism involving ·OH radical attack played the main role in both photodegradation reactions catalyzed by the as-synthesized ZnO samples, whereas the photosensitization mechanism had a negligible influence. The use of ESI-MS analyses showed that the MB dye molecules were broken up by the action of the ZnO photocatalyst, indicating the occurrence of a mineralization process.

Introduction

The inappropriate disposal of hazardous industrial wastes such as pesticides, dyes, and pharmaceuticals in water resources causes serious effects in entire ecosystems, with significant impacts on the environment and to the health of living beings.[1,2] There are increasing efforts to develop suitable processes for the elimination or reduction of such contaminants.[3–5] Oxide semiconductors including zinc oxide (ZnO) have been successfully used in photocatalytic processes for the degradation of environmental pollutants.[6] Their properties such as good chemical stability and suitable band gaps of about 3.2 eV result in efficient photocatalysis.[7] Several methods have been used to synthesize ZnO, such as the polymeric precursor method,[6] hydrothermal synthesis,[8] and the sol-gel method.[9] Among these, the polymeric precursor method offers the advantages of low cost, simplicity, and controllable chemical composition, enabling good reproducibility, a high degree of crystallinity, and high purity.[10]

Several changes in the traditional polymeric precursor method have been proposed to enhance the electronic, textural, and morphological properties of semiconductor materials. Abreu et al. showed that the introduction of certain additives in the polymeric resin could prevent the formation of bridge bonds between citric acid and the metallic cation, hence promoting the formation of particles with regular morphology.[11] Various molecules have been used as sources of nitrogen or sulfur to promote doping and improve the photocatalytic properties, with their degradation providing an environment rich in N or S during semiconductor crystallization.[12–14] However, few studies have been dedicated to investigating these effects in detail. One important aspect is the effect of different molecules with similar structures in this process, as their degradation temperatures and times vary widely, enabling the control of anion doping and particle growth.

This work therefore provides a systematic investigation of the influence of the use of two different sources of N [melamine (Mel) or urea (Ur)] during the synthesis of ZnO nanoparticles and their effects on the physicochemical and photocatalytic properties. The photoactivity of the as-synthesized ZnO samples was probed by the degradation of methylene blue (MB)

[a] G. T. S. T. da Silva,[+] Dr. O. F. Lopes[+]
Departamento de Química
Universidade Federal de São Carlos
Rodovia Washington Luiz, km 235, 13.565-905, São Carlos, SP (Brazil)

[b] G. T. S. T. da Silva,[+] Dr. K. T. G. Carvalho,[+] Dr. O. F. Lopes,[+] Dr. C. Ribeiro
Laboratório Nacional de Nanotecnologia para o Agronegócio
LNNA—Embrapa Instrumentação
Rua XV de Novembro, n° 1452, 13.561-206, São Carlos, SP (Brazil)
Fax: (+55)16-2107-2902
E-mail: caue.ribeiro@embrapa.com.br

[c] E. S. Gomes, Prof. A. R. Malagutti
Departamento de Farmácia
Universidade Federal dos Vales do Jequitinhonha e Mucuri
Rodovia MGT 367, km 583, 39.100-000, Diamantina, MG (Brazil)

[d] Prof. V. R. Mastelaro
Instituto de Física de São Carlos
Universidade de São Paulo
Avenida Trabalhador São-carlense, 400, 13566-590, São Carlos, SP (Brazil)

[e] Prof. H. A. J. L. Mourão
Instituto de Ciência e Tecnologia
Universidade Federal dos Vales do Jequitinhonha e Mucuri
Rodovia MGT 367, km 583, 39.100-000, Diamantina, MG (Brazil)

[+] These authors contributed equally to this work.

Supporting information and the ORCID identification number(s) for the author(s) of this article can be found under https://doi.org/10.1002/cctc.201700756.

dye and ethionamide (ETA) antibiotic under ultraviolet (UVC) irradiation. Finally, a mechanism was proposed to explain the photodegradation catalyzed by the as-synthesized ZnO samples.

Results and Discussion

Characterization

As shown in Figure 1, all the samples, with the exception of ZnO-Mel$_5$, exhibited similar XRD patterns in the 2θ range from 10 to 70°. These were typical of the hexagonal wurtzite ZnO
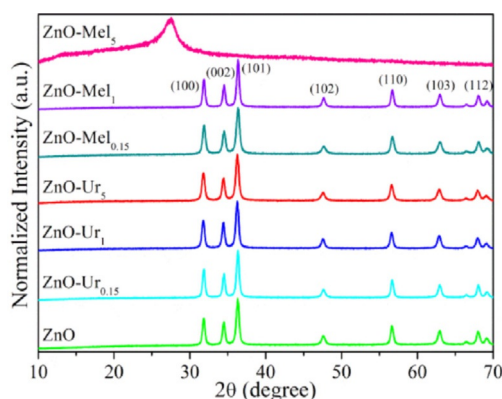

Figure 1. XRD patterns of the as-synthesized ZnO samples calcined at 550 °C.

structure, according to JCPDS card no. 36–1451. The results confirmed that all the products were well crystallized and revealed that the presence of urea in the Zn^{2+} resin did not significantly alter the crystalline structure or lead to the formation of any spurious phases. The same behavior was observed on use of smaller amounts of melamine during the synthesis. However, the use of 5.0 g of melamine resulted in the formation of another phase that was identified as graphitic carbon nitride (g-C$_3$N$_4$) (JCPDS card no. 87-1526),[5, 15, 16] which was the predominant phase in this sample.

The crystallite size of the ZnO phase was calculated by using Scherrer's equation,[17, 18] using the diffraction peaks of the $(1\,0\,0)$, $(0\,0\,2)$, and $(1\,0\,1)$ planes ($2\theta = 31.8$, 34.5, and 36.4°, respectively). As shown in Table 1, the values obtained for all the ZnO samples were very similar, with crystallite sizes of approximately 20 nm.

Table 1. Crystallite size of the ZnO samples, calculated by using Scherrer's equation.

Sample	Crystallite size (D_{hkl}) [nm]		
	31.8° $(1\,0\,0)$	34.5° $(0\,0\,2)$	36.4° $(1\,0\,1)$
ZnO	20.6	20.8	19.6
ZnO-Ur$_{0.15}$	21.5	21.6	20.9
ZnO-Ur$_1$	19.3	20.7	19.0
ZnO-Ur$_5$	18.2	18.3	17.4
ZnO-Mel$_{0.15}$	18.2	17.3	17.4
ZnO-Mel$_1$	22.6	10.8	20.9

The optical properties of the samples with only the ZnO phase were studied by UV/Visible diffuse reflectance spectroscopy. Figure 2 shows the curves of $(\alpha h\nu)^2$ as a function of photo energy ($h\nu$), from the Tauc equation,[19] for the direct
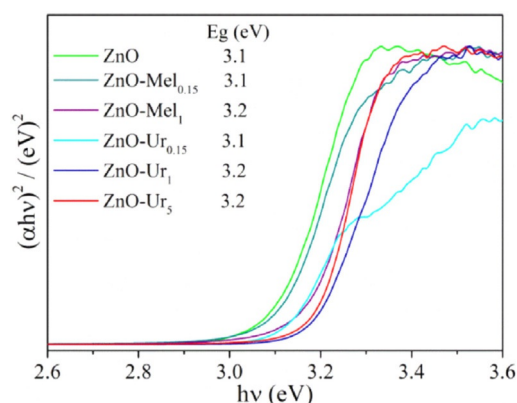

Figure 2. Tauc plot curves of the conventional ZnO, ZnO-Mel$_x$ and ZnO-Ur$_x$ samples.

band gap ZnO semiconductors.[20] The band gap energies, calculated from the x-axis intercepts of the tangent lines of the curves, were approximately 3.1–3.2 eV for all ZnO samples. The detailed results are shown in the inset of Figure 2. In summary, the presence of urea or melamine in the Zn^{2+} resin did not cause any significant changes in the electronic property of the as-synthesized ZnO samples.

As shown in Figure 3, the morphological properties of the ZnO samples were affected by the addition of the molecules of urea and melamine to the Zn^{2+} resin. The ZnO synthesized in the absence of urea and melamine consisted of rounded nanoparticles with no well-defined morphology and a broad size distribution, which could be divided into two main regions with average sizes of 35 and 110 nm, as shown in Figure 3a. On the other hand, the ZnO-Mel$_1$ and ZnO-Ur$_1$ samples consisted of nanoparticles with nearly hexagonal pyramidal shapes and sizes that were more homogeneous than for the conventional ZnO sample, with average sizes of 56 and 48 nm, respectively (Figure 3b–c). This was probably owing to the presence of the amino groups in the urea and melamine molecules, which acted as complexing agents for metal ions and consequently created a physical barrier for the sintering. This provided controlled growth of the particles, resulting in a material with greater particle size homogeneity. In summary, these molecules improve the control of the particle morphology, compared with the unmodified precursor method by using only citric acid as the complexing agent and ethylene glycol for polymerization.

Thermogravimetric analyses (TGA; Figure S1 in the Supporting Information) were performed to confirm the ZnO growth mechanism. It was observed that the presence of urea or melamine led to mass losses at higher temperatures, indicating that the production of volatiles was still occurring at temperatures that typically influence particle growth. This can be clearly seen in the DTG curves, as the main mass loss peaks were at
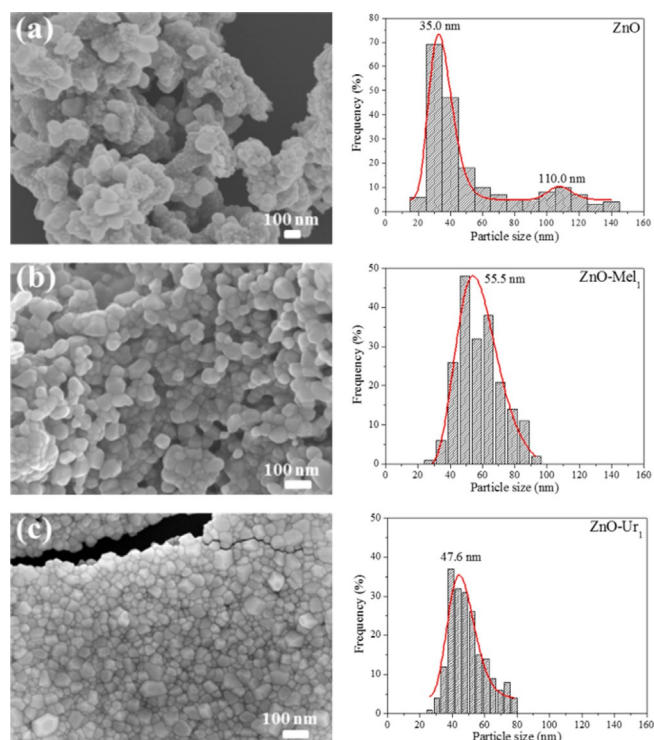
Figure 3. Representative SEM images of (a) conventional ZnO, (b) ZnO-Mel$_1$, and (c) ZnO-Ur$_1$, and their respective particle size distribution histograms. The average particle size values were calculated from the lognormal distribution parameters that fitted the particle size distribution for each sample.

higher temperatures. Hence, this organic fraction may act to prevent contact among the particles, limiting diffusion and consequently the growth itself. However, investigation of such phenomena was not the main goal of the present work, and they are only mentioned here as an additional effect.

The morphology and structure of the as-synthesized ZnO samples were further analyzed by transmission electron microscopy (TEM). As shown in Figure 4, the TEM images of all the samples revealed sphere-like ZnO nanoparticles with an average size of approximately 43 nm, in good agreement with the SEM observations (Figure 3). Furthermore, the high-resolution (HR)-TEM micrographs of the ZnO nanoparticles (Figure 4) showed crystallites with sizes of approximately 12 nm and an average inter-fringe distance of 0.28 nm, which could be attributed to the (1 0 0) plane of the hexagonal wurtzite ZnO structure. This finding confirmed the results obtained from the XRD analysis (Figure 1). Therefore, the ZnO samples are composed of polycrystalline particles with at least two crystallites.

The chemical compositions and purities of the as-synthesized ZnO samples were further characterized by FTIR analysis. As shown in Figure S2 (in the Supporting Information), the spectra exhibited similar profiles for all the ZnO samples, with absorption bands at 3445, 2923, 1634, 1386, 689, 509, and 440 cm^{-1}. All the observed absorption peaks were characteristic of a typical ZnO FTIR spectrum, without any residue of urea or melamine.[21] Bands centered at 3445 and 1634 cm^{-1} were assigned to hydroxyl groups on the ZnO surface.[21,22] A shoulder at around 2923 cm^{-1} and a small peak positioned at
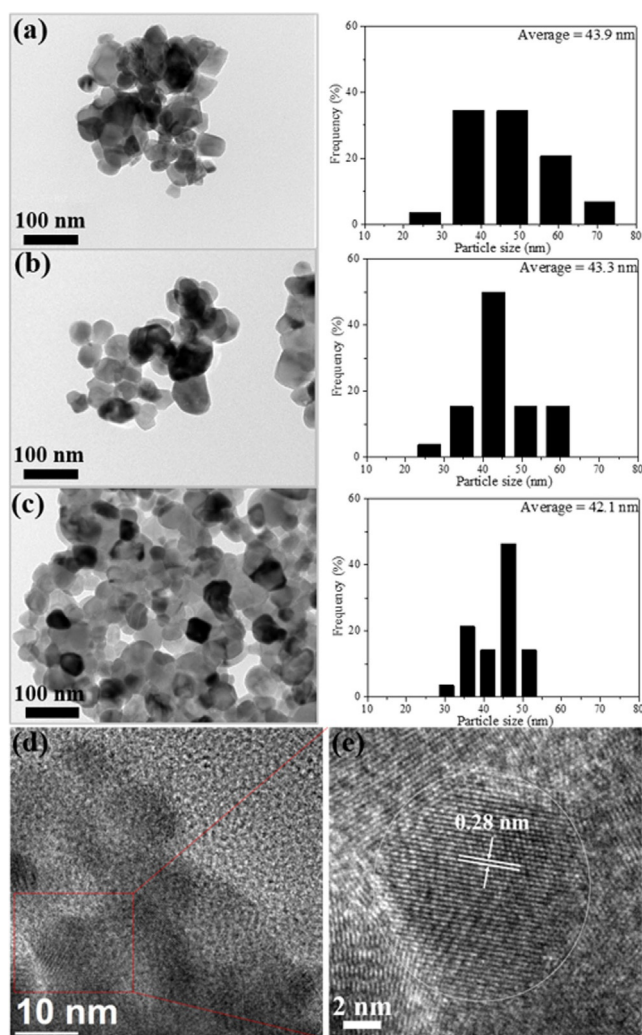

Figure 4. TEM images of the (a) conventional ZnO, (b) ZnO-Mel$_1$, and (c) ZnO-Ur$_1$ samples, and their respective particle size distribution histograms. (d–e) HR-TEM images of the ZnO.

1386 cm^{-1} were characteristic of -CH$_2$ stretching vibrations,[23] resulting from a small residual quantity of organic resin. A sharp and strong band in the range 509–440 cm^{-1} was related to the metal–oxygen stretching mode in the ZnO lattice.

Photocatalytic properties of the ZnO samples

The effect of adding urea and melamine molecules to the Zn^{2+} resin on the photocatalytic performance of the as-synthesized ZnO samples was evaluated by using the photodegradation of MB dye under UVC irradiation (Figure 5). All the ZnO samples were kept in contact with the MB dye solution in the dark for 12 h, to reach adsorption/desorption equilibrium, prior to the photocatalytic tests. It was observed that these samples exhibited negligible MB dye adsorption (< 5%), and that the direct photolysis of MB dye was also insignificant.

As shown in Figure 5, the ZnO-Mel$_x$ and ZnO-Ur$_x$ samples, especially ZnO-Mel$_1$ (Figure 5 a) and ZnO-Ur$_5$ (Figure 5 b), exhibited higher photocatalytic activities than conventional ZnO. The maximum photodegradation of MB dye catalyzed by ZnO was
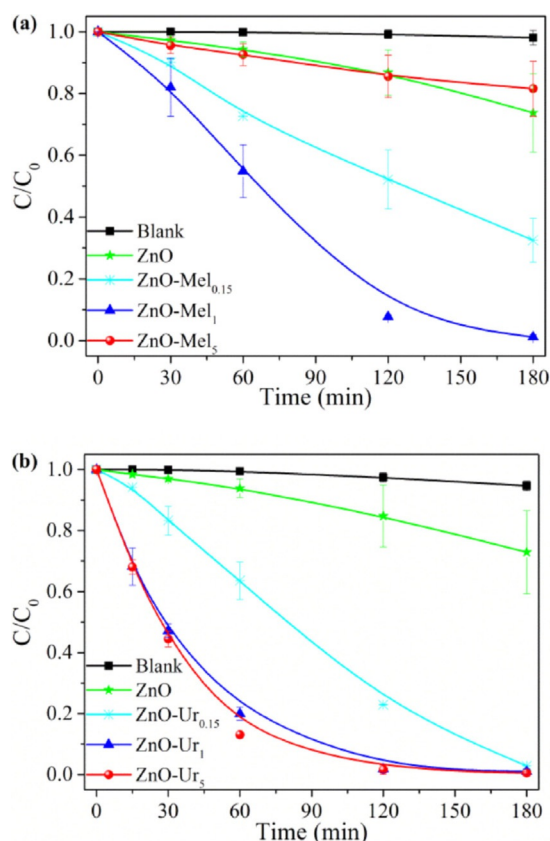
Figure 5. Kinetic curves of MB dye photodegradation catalyzed by the ZnO, ZnO-Mel$_x$ and ZnO-Ur$_x$ samples under UVC irradiation. Three independent measurements were performed to estimate the standard deviation.

kinetics should be dependent on the concentration of MB dye and the active sites of the photocatalyst. However, as the concentration of active sites remained constant throughout the degradation period, the rate law could be written as a pseudo-first-order equation, as discussed in detail in our previous work.[24] Hence, the photodegradation rate constants were obtained by using the equation: $-\ln(C/C_0) = kt$, in which C_0 and C are the concentrations of the pollutant at the start of the process and at reaction time "t", respectively, and k is the rate constant. This analysis clearly showed that an increase in the amount of melamine in the Zn^{2+} resin from 0.15 to 1.0 g resulted in a substantial improvement in photocatalytic performance, with the rate constant obtained if using ZnO-Mel$_1$ approximately 4.1 times higher than with the ZnO-Mel$_{0.15}$ sample. However, a further increase in the amount of melamine in the Zn^{2+} resin, from 1.0 to 5.0 g, resulted in the predominant formation of g-C$_3$N$_4$ (Figure 1), which typically exhibits a lower photoactivity than ZnO samples under UVC irradiation. Therefore, this sample did not follow the expected trend. Notably, the g-C$_3$N$_4$ sample (ZnO-Mel$_5$) was outside the scope of this study. In the case of the ZnO-Ur$_x$ samples, photocatalytic performance increased progressively according to the amount of urea used (ZnO-Ur$_{0.15}$ < ZnO-Ur$_1$ < ZnO-Ur$_5$), with the ZnO-Ur$_5$ sample presenting a rate constant approximately 2.8 times higher than obtained for ZnO-Ur$_{0.15}$.

The observed behavior suggested that the photocatalytic properties of the ZnO nanoparticles could be optimized by adjusting the amount of urea or melamine used in the synthesis. In addition, the higher photocatalytic activities obtained for the ZnO-Ur$_x$ samples, compared with the corresponding ZnO-Mel$_x$ samples, indicated that urea was more effective in improving the properties of the ZnO.

The main parameters that govern the catalytic performance of a photocatalyst are: (i) electronic properties including the band gap and lifetime of charge carriers; (ii) morphological properties involving the shape and size of the particles; and (iii) textural properties and the degree of hydroxylation and reactivity of the surface.[25–28] To obtain a better understanding of the photocatalytic activities of the ZnO, ZnO-Mel$_1$, and ZnO-Ur$_5$ samples, some physical-chemical properties were further evaluated by using N$_2$ adsorption/desorption, Fourier transform infrared spectroscopy (FTIR), and X-ray photoelectron spectroscopy (XPS).

Although the Brunauer–Emmett–Teller (BET) specific surface areas were similar for all the materials (Table 3), the mesoporous volumes of the ZnO-Ur$_5$ and ZnO-Mel$_1$ samples were approximately 2.4 and 3.0 times higher, respectively, compared

approximately 6%, whereas values of 87% and 45% were obtained for the ZnO-Ur$_5$ and ZnO-Mel$_1$ samples, respectively, after 60 min of reaction. Almost complete photodegradation of the MB dye was achieved after 120 min if using both of these samples. It could therefore be concluded that the inclusion of urea or melamine in the ZnO synthesis significantly improved the photocatalytic properties of the as-synthesized ZnO samples. Additionally, all the ZnO-Ur$_x$ samples showed complete MB dye discoloration after 180 min, whereas different behavior was observed for the ZnO-Mel$_x$ samples. Figure S3 (in the Supporting Information) shows the visible spectra and photographs showing the changes in color of the MB dye solution after different periods of the photocatalytic reaction in the absence and presence of the ZnO-Ur$_5$ sample.

Similar conclusions could be reached from the reaction rate constants shown in Table 2. It was expected that the reaction

Table 2. Kinetic rate constants (k_{MB}) for MB dye photodegradation.

Sample	$k_{MB} \times 10^3$ [min^{-1}]	Sample	$k_{MB} \times 10^3$ [min^{-1}]
Pure MB	0.1	ZnO	1.7
ZnO-Mel$_{0.15}$	6.3	ZnO-Ur$_{0.15}$	12.5
ZnO-Mel$_1$	26.0	ZnO-Ur$_1$	33.4
ZnO-Mel$_5$	1.1	ZnO-Ur$_5$	35.1

Table 3. Textural properties of the as-synthesized ZnO samples.

Sample	SSA[a] [m^2 g^{-1}]	V_{pores}[b] [cm^3 g^{-1}]
ZnO	10.3	0.05
ZnO-Mel$_1$	8.7	0.15
ZnO-Ur$_5$	7.8	0.12

[a] SSA: BET specific surface area. [b] V_{pores}: mesopore volume.

with the conventional ZnO sample, indicating enhanced access to the surface active sites of ZnO-Ur$_5$ and ZnO-Mel$_1$. This effect could have contributed to increasing the activity of the ZnO samples towards photodegradation of the MB dye.

It is well known that the quantity of surface -OH groups plays an important role in photocatalytic processes,[29,30] especially if the hydroxyl radical is the major active species involved in the oxidation of an organic pollutant. As discussed previously, the absorption peak at 3445 cm^{-1} is related to the -OH surface groups and its intensity is proportional to the concentration of these groups on the surface of the material.[29–31] A semi-quantitative analysis of these groups was therefore performed for each sample (Figure 6), with band normalization using the most intense spectrum as the reference. The ZnO-Ur$_5$ sample, which showed the greatest quantity of surface -OH groups, was used as the reference, and the ZnO-Mel$_1$ and ZnO samples presented intensities that were approximately 13% and 32% lower, respectively, compared with ZnO-Ur$_5$. These results were in agreement with the highest photocatalytic performance of the ZnO-Ur$_5$ sample.

XPS analysis was performed to investigate the surface composition and chemical state of the elements, and to confirm the N-doping of the ZnO-Mel$_1$ and ZnO-Ur$_5$ samples. The survey spectra of the ZnO samples (Figure 7a) confirmed the presence of the elements Zn and O on the surfaces of all the samples, without any contamination. For all the samples, the Zn2p XPS high-resolution spectra (Figure 7b) showed a peak at 1022 eV related to the binding energy of Zn2p$_{3/2}$. The O1s XPS high-resolution spectra (Figure 7c) exhibited broad and asymmetric peaks that were deconvoluted by employing a Gaussian curve fitted to two peaks at 530.6 and 531.9 eV, attributed to the O—Zn and O—H bonds, respectively. High-resolution N1s XPS spectra of the ZnO, ZnO-Mel$_1$, and ZnO-Ur$_5$ samples (Figure 7d) were also collected to determine if N from urea or melamine was incorporated in the ZnO structure. As expected, no peaks related to
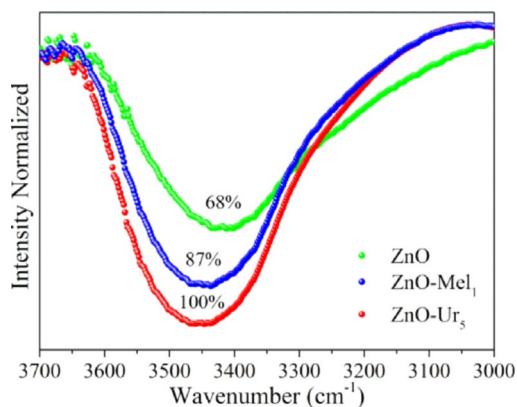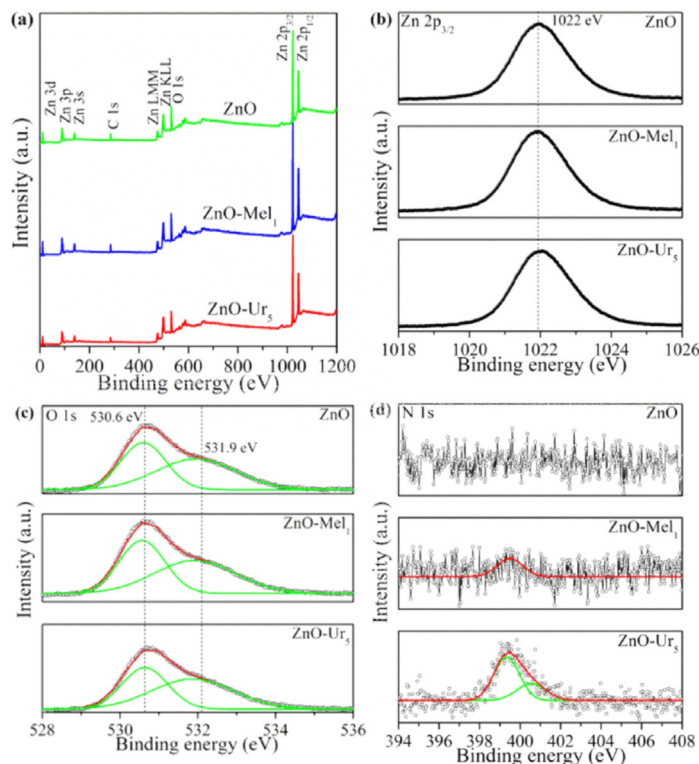

Figure 7. X-ray photoelectron spectra of the ZnO, ZnO-Mel$_1$, and ZnO-Ur$_5$ samples: survey spectra (a) and high-resolution spectra for (b) Zn2p, (c) O1s, and (d) N1s.

nitrogen bonds were observed for the conventional ZnO sample. For the ZnO-Mel$_1$ sample, the peak attributed to nitrogen was hard to identify, owing to a low signal/noise ratio. A more intense asymmetric peak at about 400 eV was observed in the N1s XPS spectrum of the ZnO-Ur$_5$ sample and was fitted by using two peaks at 399.5 and 400.6 eV. The peak at 399.5 eV was assigned to the Zn—N linkage resulting from the incorporation of anionic nitrogen into the ZnO crystal lattice, replacing the oxygen atoms.[9,32] The peak at 400.6 eV was attributed to oxidized nitrogen in the form of Zn-O-N or Zn-N-O linkages.[13,33] Notably, a higher intensity N1s peak was exhibited by the ZnO-Ur$_5$ sample, compared with ZnO-Mel$_1$, indicating that the former had a greater N content. The N-doping of ZnO positively affected the electronic properties of the materials, as the ZnO-Ur$_5$ and ZnO-Mel$_1$ samples exhibited enhanced photocatalytic properties.

In summary, the greater photoactivities of the ZnO-Ur$_x$ and ZnO-Mel$_x$ samples, compared with ZnO, were probably owing to three main factors: (i) improved textural properties, associated with increased surface hydroxyl groups; (ii) smaller and more homogeneous particles; and (iii) the incorporation of N into the ZnO lattice, which provided better electronic properties.

Study of the MB dye degradation mechanism

ZnO has been extensively used as a photocatalyst in reactions concerning the degradation of organic pollutants, artificial photosynthesis, and others.[6,34] However, only a few studies

Figure 6. Normalized FTIR spectra in the -OH surface groups region (3700–3000 cm^{-1}).

have attempted to elucidate the mechanisms of the photocatalytic reactions and identify the active species involved in the process. Therefore, investigation was made of the roles of the different mechanisms (indirect, direct, and photosensitization)[27,35,36] of the MB photodegradation under UVC irradiation, by using the ZnO, ZnO-Ur$_5$, and ZnO-Mel$_1$ photocatalysts.

The contribution of the indirect mechanism (·OH radical formation and attack) was evaluated by determination of ·OH by using terephthalic acid (TPA) as a target molecule. The reaction between the ·OH radical and TPA generates a fluorescent product, 2-hydroxyterephthalic acid (HTPA), which is easily monitored by the photoluminescence (PL) technique. The amount of HTPA formed is directly proportional to the quantity of ·OH radicals generated by the irradiated photocatalyst. The PL spectra of HTPA obtained after 30 min on using the as-synthesized ZnO samples under UVC irradiation are shown in Figure 8 a. The quantity of photogenerated ·OH radicals was significantly higher if the ZnO-Ur$_5$ sample was used as a photocatalyst, followed by the ZnO-Mel$_1$ and ZnO samples. The highest amount of hydroxyl radicals generated by the ZnO-Ur$_5$ sample was a result of its improved electronic structure, as well as the large quantity of hydroxyl groups on its surface.

The reaction between TPA and the ·OH radical is only dependent on diffusion of the ·OH radicals in the solution, so the quantity of photogenerated ·OH radicals is directly propo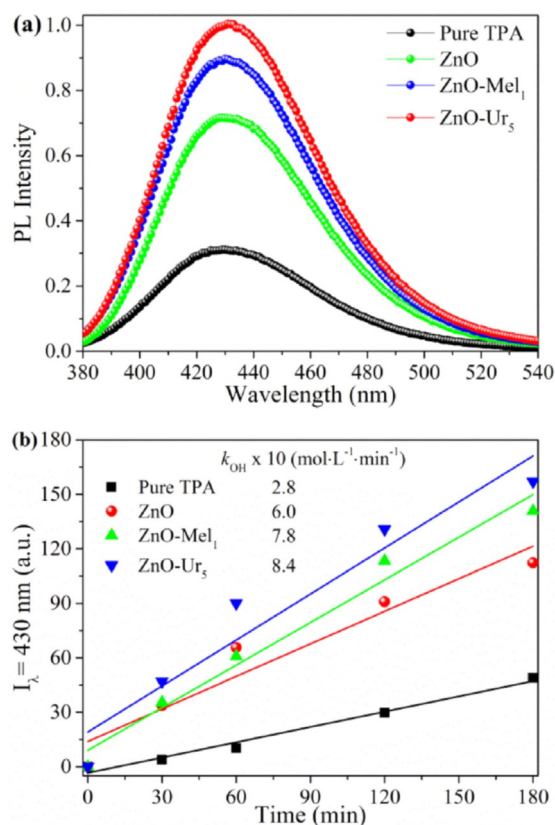rtional to the amount of HTPA formed. Hence, the kinetic constants for formation of HTPA and ·OH radicals are similar,[30,37–39] so the rate constant for ·OH radical (k_{OH}) generation could be obtained by applying the pseudo-zero-order reaction equation to the HTPA formation data (Figure 8 b). The highest rate constant was found for the ZnO-Ur$_5$ sample, followed by the ZnO-Mel$_1$ and ZnO samples. Therefore, the rate constants for ·OH radical formation and for organic pollutants photodegradation, both catalyzed by the as-synthesized ZnO samples, exhibited the same trend (Figure S4 in the Supporting Information). These results strongly indicated that the indirect mechanism played a major role in the photodegradation process, as the order of ·OH radical formation followed the order of photoactivity for the ZnO samples.

The photo-oxidation of the MB dye molecules catalyzed by the ZnO-Ur$_5$ sample was confirmed by analysis of the MB solution by using electrospray ionization mass spectrometry (ESI-MS). The ESI-MS spectrum for the MB dye standard solution (Figure 9 a) only exhibited a strong signal at a mass/charge (m/z) ratio of 284, attributed to the MB structure without any oxidation. After 120 min of UVC irradiation in the presence of the ZnO-Ur$_5$ photocatalyst, the ESI-MS spectrum for the MB dye solution (Figure 9 b) exhibited several peaks at $m/z = 332$, 318, 301, 284, 270, 256, 243, 162, and 129. Furthermore, the intensity of the signal at $m/z = 284$ was lower than in the spectrum for pure MB dye, indicating a decrease in its proportion following the formation of other species. The signals at $m/z = 301$,
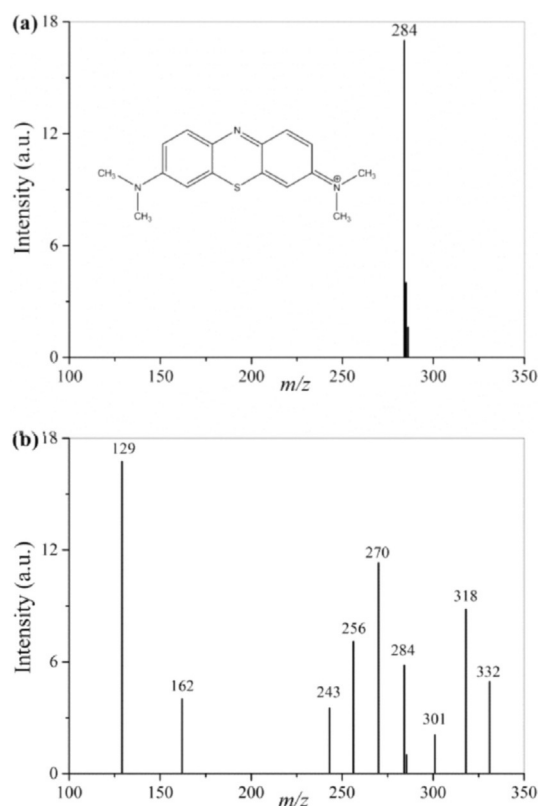

Figure 8. (a) PL spectra for 2-hydroxyterephthalic acid formation after 30 min under UVC irradiation, on using the ZnO, ZnO-Mel$_1$, and ZnO-Ur$_5$ photocatalysts. (b) Pseudo-zero-order kinetics for indirect formation of hydroxyl radicals by the samples.

Figure 9. ESI mass spectra of (a) pure MB dye and (b) MB dye after photodegradation catalyzed by the ZnO-Ur$_5$ sample during 120 min under UVC irradiation.

318, and 332 reflected successive hydroxylation in the aromatic ring of the MB molecule, confirming that the ·OH radical played an important role in the MB dye photodegradation reaction, under the conditions used. The signals at $m/z = 270$, 256, and 243 reflected the loss of one or more methyl substituents from the amine groups of MB, forming the azure B, azure A, and azure C species, respectively.[40] Additionally, signals at $m/z = 129$ and 162 corresponded to cleavage of the aromatic ring resulting from attack by active species that were photogenerated in the presence of the ZnO-Ur$_5$ sample under UVC irradiation. Notably, this last finding confirmed that the MB dye molecules were broken down by using the photocatalyst, which was a strong indication of the occurrence of a mineralization process. This finding was very important, because a good catalyst must be able to break down the contaminant molecule, while at the same time minimizing the possible formation of byproducts that could also be toxic. Based on the ESI-MS results, a schematic diagram (Figure S5 in the Supporting Information) was proposed to clearly describe the mechanism of the MB dye photodegradation catalyzed by the as-synthesized ZnO samples.

The stability of a photocatalyst is a crucial parameter in catalytic applications such as the treatment of wastewater.[41] Therefore, the photostability of the conventional ZnO and ZnO-Ur$_5$ samples was evaluated by performing recycling experiments for 180 min under UVC irradiation. As shown in Figure 10, no significant deactivation ($< 5\%$) was observed for both photocatalysts, even after four successive re-uses for MB dye photodegradation.

The structural, electronic, and morphological properties of the ZnO-Ur$_5$ photocatalyst were analyzed by the XRD, UV/Vis diffuse reflectance spectroscopy (DRS), and SEM techniques, before and after MB dye degradation for 180 min under UVC irradiation. There were no significant changes in the XRD pattern or the SEM image of the used ZnO-Ur$_5$ sample compared to the fresh material (Figure S6 in the Supporting Information). The band gap value of the used sample showed a slight increase, from 3.15 to 3.21 eV, which could be attributed to experimental error. These results revealed that the photocatalyst exhibited high structural, electronic, and morphological stability during the photocatalytic reaction under the conditions employed.
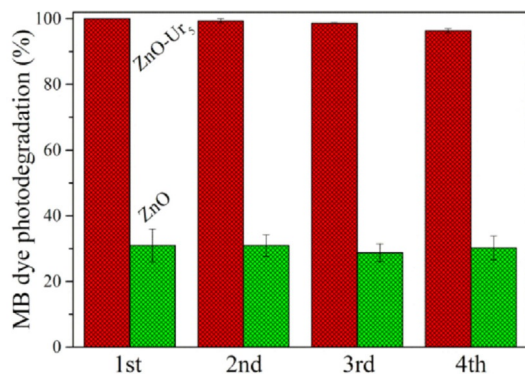

Figure 10. Stability of the conventional ZnO and ZnO-Ur$_5$ photocatalysts during four cycles of MB dye photodegradation.

Photodegradation of ethionamide (ETA) antibiotic

Ethionamide (ETA), a first-line antibiotic used for the treatment of tuberculosis, was employed here as a model of a real organic pollutant, with maximum absorption centered at 289 nm in the ultraviolet region (Figure S7 in the Supporting Information).[42] Figure 11 a shows the kinetic curves for ETA
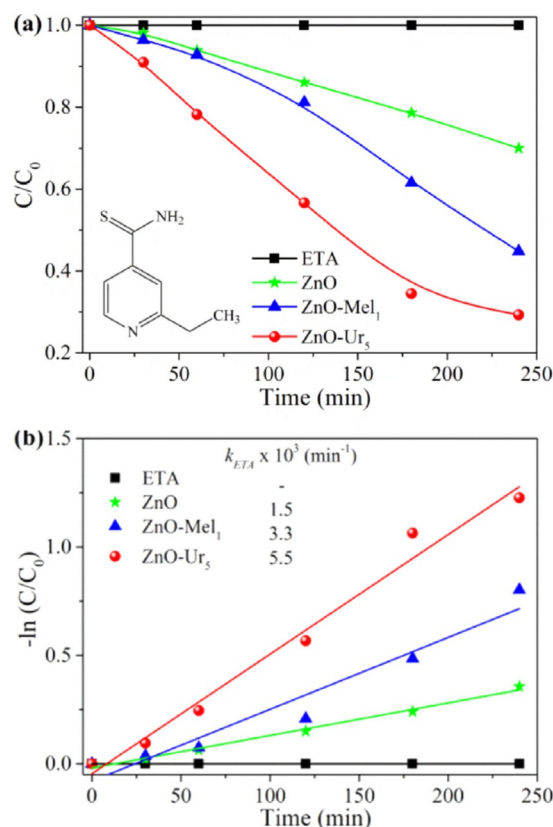

Figure 11. (a) Kinetic curves of ethionamide photodegradation catalyzed by the ZnO, ZnO-Mel$_1$, and ZnO-Ur$_5$ samples under UVC irradiation. (b) First-order kinetics of ethionamide degradation catalyzed by the as-synthesized samples.

photodegradation catalyzed by the as-synthesized ZnO samples under UVC irradiation. The photodegradation curves linearized by pseudo-first-order kinetics are shown in Figure 11 b, and the rate constant (k_{ETA}) values are provided in the inset of Figure 11 b. All the as-synthesized ZnO samples exhibited ETA photodegradation activity and negligible ETA adsorption ($< 5\%$), and the direct photolysis of this molecule was insignificant. The k_{ETA} values calculated for ETA degradation in the presence of the ZnO-Ur$_5$ and ZnO-Mel$_1$ photocatalysts were approximately 3.7 and 2.2 times higher, respectively, compared with the value obtained for conventional ZnO. The ratio of the effectiveness of these samples was the same as for MB dye photodegradation (k_{MB}) and for ·OH radical generation (k_{OH}), indicating that the main degradation mechanism was also owing to the attack of hydroxyl radicals on the ETA molecules. Thus, these results suggested that photosensitization was not the main factor responsible for photodegradation of the studied

organic pollutants (MB and ETA) catalyzed by the as-synthesized ZnO samples, and that the degradation process was independent of the target molecule. In summary, the as-synthesized ZnO photocatalysts exhibited excellent potential for application in real photocatalytic processes to degrade any type of organic pollutant. Table S1 (in the Supporting Information) provides a comparison of the photoactivities of different photocatalysts and ZnO-Ur$_5$ for MB dye degradation under identical experimental conditions (i.e., light source, photocatalyst amount, MB dye concentration, and reactor design). This comparison demonstrates the excellent performance of the ZnO-Ur$_5$ photocatalyst.

Conclusions

It was found that ZnO samples prepared by using a modified polymeric precursor method with addition of urea (ZnO-Ur$_x$) or melamine (ZnO-Mel$_x$) exhibited higher photocatalytic efficiencies for degradation of organic pollutants compared with ZnO obtained conventionally. The use of these molecules (melamine and urea) in the synthesis provided controlled growth of the ZnO particles, resulting in materials with more homogeneous particle sizes. The enhanced performance of ZnO-Ur$_x$ and ZnO-Mel$_x$ in the degradation of MB dye and ETA antibiotic was explained by the greater quantity of surface hydroxyl groups, the incorporation of nitrogen into the ZnO lattice, and the enhanced textural properties of the materials. These positive effects were most pronounced in the case of the ZnO-Ur$_x$ samples. Investigation of the photocatalysis mechanism showed that degradation of the pollutants over all the photocatalysts proceeded mainly by means of non-selective ˙OH radical attack, and that the photosensitization mechanism exerted a negligible effect. Additionally, the results of ESI-MS analysis demonstrated that the MB dye molecules were oxidized by the action of the ZnO photocatalyst, which was indicative of a mineralization process.

Experimental Section

Reagents

The chemicals used were zinc acetate (Zn(CH$_3$COO)$_2$·2H$_2$O, $\geq$98 wt%, Synth), citric acid (HOC(CO$_2$H)(CH$_2$CO$_2$H)$_2$, $>$99 wt%, Quemis), ethanol (CH$_3$CH$_2$OH, $\geq$99.5 wt%, Quemis), ethylene glycol (HOCH$_2$CH$_2$OH, $>$99 wt%, Synth), nitric acid (HNO$_3$, Êxodo Científica), melamine (C$_3$N$_6$H$_6$, 99 wt%, Sigma–Aldrich), urea (CH$_4$N$_2$O, $>$99 wt%, Synth), methylene blue (C$_{16}$H$_{18}$N$_3$SCl, Vetec), ethionamide (C$_8$H$_{10}$N$_2$S, 98 wt%, Sigma–Aldrich), sodium hydroxide (NaOH, Synth), and terephthalic acid (C$_6$H$_4$(COOH)$_2$, 98 wt%, Aldrich). All reagents were used as received, without further purification.

Synthesis of materials

The polymeric citrate precursor method was used to synthesize the ZnO samples. In a typical procedure, zinc acetate (5 g, 0.023 mol) and citric acid (13 g, 0.068 mol) were dissolved in ethanol (200 mL, 3.43 mol) and ethylene glycol (8 mL, 0.143 mol) at 70 °C. Then, HNO$_3$ (6 mL) was added to the mixture to complete dissolution. The volume of the solution obtained was reduced by

evaporation by using a hotplate at 90 °C for 30 min, under magnetic stirring, resulting in a viscosity of approximately 5.5 cP. This resulting solution is referred to as the Zn^{2+} resin. Finally, seven ZnO samples were obtained by heat treatment of the Zn^{2+} resin in an electric furnace, by using the following parameters: heating at a rate of 2 °C min^{-1} until 100 °C and holding at this temperature for 1 h; heating at 3 °C min^{-1} until 300 °C and holding at this temperature for 2 h to remove the organic portion; and heating at 3 °C min^{-1} until 550 °C and holding at this temperature for 2 h to obtain fully crystallized ZnO nanoparticles. A conventional ZnO sample (referred to as ZnO) was obtained from 11 mL of pure Zn^{2+} resin. Another six samples were obtained by adding different weight amounts of melamine (Mel) or urea (Ur), that is, 0.15 g, 1.0 g, and 5.0 g, to 11 mL of Zn^{2+} resin. These samples are referred to as ZnO-Mel$_x$ or ZnO-Ur$_x$, in which x is the weight of added Mel or Ur molecules.

Characterization

X-ray diffraction (XRD) measurements were performed with a Shimadzu XRD 6000 diffractometer, using nickel-filtered CuK$_\alpha$ radiation, 2θ from 10° to 70° in continuous scanning mode, and a step width of 0.02°. UV/Vis diffuse reflectance spectra (DRS) were recorded from 200 to 800 nm by using a Shimadzu UV-2600 spectrophotometer equipped with an integrating sphere (ISR-2600 Plus). Magnesium oxide (MgO) powder was used as a reflectance standard. Fourier transform infrared (FTIR) spectra were recorded from 4000 to 500 cm^{-1} by using a Bruker Vertex 70 spectrophotometer, with a resolution of 4 cm^{-1} and averaging of 32 scans. The samples were mixed with potassium bromide in a mass ratio of 1:100 (ZnO/KBr) and then pressed to form thin discs. Scanning electron microscopy (SEM) images were obtained with a JEOL JSM-6701F field emission instrument. Transmission electron microscopy (TEM) images were obtained with a FEI Tecnai G2 F20 microscope operated at 200 kV. Thermogravimetric analyses (TGA) were performed with a Shimadzu TGA-50 equipment by using oxidative atmosphere conditions (air flow rate of 60 mL min^{-1}), temperature range from 30 to 600 °C, and heating rate of 10 °C min^{-1}. Specific surface area (SSA) values were calculated according to the Brunauer–Emmett–Teller (BET) method, by using N$_2$ adsorption data obtained at -196 °C with a Micromeritics ASAP-2020 system. Samples were previously treated (degassed) by heating at 80 °C under vacuum until reaching a degassing pressure lower than 20 μm Hg. X-ray photoelectron spectroscopy (XPS) was performed by using a ScientaOmicron ESCA+ spectrometer with a high-performance hemispheric analyzer (EA 125), using monochromatic AlK$_\alpha$ ($h\nu =$ 1486.6 eV) radiation as the excitation source. The operating pressure in the ultra-high-vacuum (UHV) chamber during the analysis was 2×10^{-9} mbar. Energy steps of 50 and 20 eV were used for the survey and high-resolution spectra, respectively. The following peaks were used for the quantitative analysis: O 1s, C 1s, N 1s, and Zn 2p. The C (C, H) component of the C 1s peak of adventitious carbon was fixed at 284.5 eV to set the bond energy scale, and treatment of the data employed CasaXPS software.

Photocatalytic tests

The photoactivity of the ZnO samples was evaluated in the degradation of methylene blue (MB) dye under ultraviolet (UVC) irradiation. In a typical procedure, photocatalyst (10 mg) was placed in contact with an aqueous solution of MB (20 mL, 10 mg L^{-1}). All the experiments employed a photoreactor[38] equipped with six UVC lamps (Philips TUV, 15 W, maximum emission at 254 nm and

average light intensity of 40 W m^{-2}; see the spectral distribution in Figure S8 in the Supporting Information), a magnetic stirrer, and a heat exchanger that maintained the temperature at 18 °C. The photodegradation of the MB dye was monitored at regular intervals by using a Shimadzu UV-1601 PC spectrophotometer in the visible range, as this molecule exhibits maximum absorbance at 654 nm. Before the kinetic experiments, the suspensions were kept in the dark for 12 h to establish adsorption/desorption equilibrium of the dye on the photocatalyst surface. The same conditions were used to evaluate the activity of the as-synthesized ZnO samples in the degradation of ethionamide antibiotic (2-ethylpyridine-4-carbo-thioamide, ETA). The initial concentration of ETA was 10 mg L^{-1} and its decreasing concentration was monitored at 289 nm.

Mass spectrometry (MS) was employed to elucidate the mechanism of oxidation of MB dye and the formation of byproducts during the photocatalytic process, by using the ZnO sample with the highest activity. The solutions were monitored by using electrospray ionization mass spectrometry (ESI-MS, Varian 310-MS), in positive ion mode. Aliquots were introduced into the ESI source by using a syringe pump and a flow of N$_2$ was maintained at 20 mL min^{-1}. The products are referred to by using the *m/z* ratio of the protonated molecular ion.

Hydroxyl radical formation tests

The ability of each ZnO photocatalyst to form hydroxyl radicals ($^\bullet$OH) under UVC irradiation was indirectly determined by the photoluminescence technique, by using terephthalic acid (TPA) as the target molecule.[30,37,38] The reaction between photogenerated $^\bullet$OH radicals and TPA results in the formation of 2-hydroxyterephthalic acid (HTPA), which is fluorescent.[30,37,38] Hence, the HTPA concentration is proportional to the $^\bullet$OH radical concentration. In these experiments, ZnO photocatalyst (10 mg) was placed in contact with a solution of TPA (20 mL, 5×10^{-4} mol L^{-1}) prepared in aqueous NaOH (2×10^{-3} mol L^{-1}). All experiments were performed by using the photoreactor described in the last section. At regular intervals, the HTPA concentration was monitored by fluorescence measurements by using a Shimadzu RF-5301PC spectrofluorophotometer. The fluorescence emission spectrum in the wavelength range 380–540 nm ($\lambda_{maximum}=430$ nm) was obtained by using excitation at 315 nm.

Acknowledgments

Conflict of interest

The authors declare no conflict of interest.

[1] M. Chen, W. Chu, *J. Hazard. Mater.* **2012**, *219–220*, 183–189.
[2] H. Dong, G. Chen, J. Sun, C. Li, Y. Yu, D. Chen, *Appl. Catal. B* **2013**, *134–135*, 46–54.
[3] C. Li, G. Chen, J. Sun, J. Rao, Z. Han, Y. Hu, W. Xing, C. Zhang, *Appl. Catal. B* **2016**, *188*, 39–47.
[4] C. Li, G. Chen, J. Sun, H. Dong, Y. Wang, C. Lv, *Appl. Catal. B* **2014**, *160–161*, 383–389.
[5] G. T. S. T. da Silva, K. T. G. Carvalho, O. F. Lopes, C. Ribeiro, *Appl. Catal. B* **2017**, *216*, 70–79.
[6] K. T. G. Carvalho, S. C. Fidelis, O. F. Lopes, C. Ribeiro, *Ceram. Int.* **2015**, *41*, 10587–10594.
[7] K. M. Lee, C. W. Lai, K. S. Ngai, J. C. Juan, *Water Res.* **2016**, *88*, 428–448.
[8] J. Yu, X. Yu, *Environ. Sci. Technol.* **2008**, *42*, 4902–4907.
[9] J. J. Macías-Sánchez, L. Hinojosa-Reyes, A. Caballero-Quintero, W. de la Cruz, E. Ruiz-Ruiz, A. Hernández-Ramírez, J. L. Guzmán-Mar, *Photochem. Photobiol. Sci.* **2015**, *14*, 536–542.
[10] N. L. V. Carreño, E. R. Leite, L. P. S. Santos, P. N. Lisboa-Filho, E. Longo, G. C. L. Araújo, A. Barison, A. G. Ferreira, A. Valentini, L. F. D. Probst, *Quim. Nova* **2002**, *25*, 935–942.
[11] A. Abreu Jr., S. M. Zanetti, M. A. S. Oliveira, G. P. Thim, *J. Eur. Ceram. Soc.* **2005**, *25*, 743–748.
[12] N. P. Herring, L. S. Panchakarla, M. S. El-Shall, *Langmuir* **2014**, *30*, 2230–2240.
[13] I. M. P. Silva, G. Byzynski, C. Ribeiro, E. Longo, *J. Mol. Catal. A* **2016**, *417*, 89–100.
[14] J. J. L. Hmar, T. Majumder, S. Dhar, S. P. Mondal, *Thin Solid Films* **2016**, *612*, 274–283.
[15] Y. He, Y. Wang, L. Zhang, B. Teng, M. Fan, *Appl. Catal. B* **2015**, *168–169*, 1–8.
[16] K. T. G. Carvalho, A. E. Nogueira, O. F. Lopes, G. Byzynski, C. Ribeiro, *Ceram. Int.* **2017**, *43*, 3521–3530.
[17] A. L. Patterson, *Phys. Rev.* **1939**, *56*, 978–981.
[18] J. I. Langford, A. J. C. Wilson, *J. Appl. Crystallogr.* **1978**, *11*, 102–113.
[19] J. Tauc, *Mater. Res. Bull.* **1970**, *5*, 721–730.
[20] S. Anandan, N. Ohashi, M. Miyauchi, *Appl. Catal. B* **2010**, *100*, 502–509.
[21] Z. Dai, K. Liu, Y. Tang, X. Yang, J. Bao, J. Shen, *J. Mater. Chem.* **2008**, *18*, 1919–1926.
[22] J. Singh, P. Kumar, K. S. Hui, K. N. Hui, K. Ramam, R. S. Tiwari, O. N. Srivastava, *CrystEngComm* **2012**, *14*, 5898–5904.
[23] Y. Chen, H. Zhao, B. Liu, H. Yang, *Appl. Catal. B* **2015**, *163*, 189–197.
[24] V. R. de Mendonça, H. A. J. L. Mourão, A. R. Malagutti, C. Ribeiro, *Photochem. Photobiol.* **2014**, *90*, 66–72.
[25] H. A. J. L. Mourão, V. R. de Mendonça, A. R. Malagutti, C. Ribeiro, *Quim. Nova* **2009**, *32*, 2181–2190.
[26] O. F. Lopes, V. R. de Mendonça, F. B. F. Silva, E. C. Paris, C. Ribeiro, *Quim. Nova* **2014**, *38*, 106–117.
[27] M. A. Henderson, *Surf. Sci. Rep.* **2011**, *66*, 185–297.
[28] U. I. Gaya, A. H. Abdullah, *J. Photochem. Photobiol. C* **2008**, *9*, 1–12.
[29] V. R. de Mendonça, O. F. Lopes, R. P. Fregonesi, T. R. Giraldi, C. Ribeiro, *Appl. Surf. Sci.* **2014**, *298*, 182–191.
[30] O. F. Lopes, E. C. Paris, C. Ribeiro, *Appl. Catal. B* **2014**, *144*, 800–808.
[31] J. Bertaux, F. Froehlich, P. Ildefonse, *J. Sediment. Res.* **1998**, *68*, 440–447.
[32] M. Wang, F. Ren, J. Zhou, G. Cai, L. Cai, Y. Hu, D. Wang, Y. Liu, L. Guo, S. Shen, *Sci. Rep.* **2015**, *5*, 12925.
[33] S. A. Bakar, G. Byzynski, C. Ribeiro, *J. Alloys Compd.* **2016**, *666*, 38–49.
[34] G. Byzynski, C. Melo, D. P. Volanti, M. M. Ferrer, A. F. Gouveia, C. Riberio, J. Andrés, E. Longo, *Materials and Design* **2017**, *120*, 363–375
[35] Y. Mao, C. Schoeneich, K. Asmus, *J. Phys. Chem.* **1991**, *95*, 10080–10089.
[36] K. Ishibashi, A. Fujishima, *J. Photochem. Photobiol. A* **2000**, *134*, 139–142.
[37] K. Ishibashi, A. Fujishima, T. Watanabe, K. Hashimoto, *Electrochem. Commun.* **2000**, *2*, 207–210.
[38] O. F. Lopes, K. T. G. Carvalho, G. K. Macedo, V. R. de Mendonça, W. Avansi, C. Ribeiro, *New J. Chem.* **2015**, *39*, 6231–6237.
[39] O. F. Lopes, K. T. G. Carvalho, A. E. Nogueira, W. Avansi, C. Ribeiro, *Appl. Catal. B* **2016**, *188*, 87–97.

[40] A. Petzer, B. H. Harvey, G. Wegener, J. P. Petzer, *Toxicol. Appl. Pharmacol.* **2012**, *258*, 403 – 409.

[41] H. Dong, G. Chen, J. Sun, Y. Feng, C. Li, C. Lv, *Chem. Commun.* **2014**, *50*, 6596 – 6599.

[42] B. R. L. Ferraz, F. R. F. Leite, B. L. Batista, A. R. Malagutti, *J. Braz. Chem. Soc* **2016**, *27*, 677 – 684.